Arabian Journal of Chemistry (2023) **16**, 105201

King Saud University

Arabian Journal of Chemistry

www.ksu.edu.sa
www.sciencedirect.com

ORIGINAL ARTICLE

$CuMn_2O_4/Mn_2O_3$ micro composites: Sol- gel synthesis in the presence of sucrose and investigation of their photocatalytic properties

Azam Sobhani

Department of Chemistry, Kosar University of Bojnord, Bojnord, P. O. Box. 94104455, Iran

Received 10 March 2023; accepted 9 August 2023
Available online 15 August 2023

KEYWORDS

Micro composites;
$CuMn_2O_4$;
Sol-gel synthesis;
Photocatalyst;
Copper manganese oxide;
Magnetic property

Abstract The treatment of effluents using adsorption of pollution of solvent is a necessary aspect of research. The use of photocatalysts for this purpose has received much attention from researchers. In current research, the micro composites based on copper manganese oxides were synthesized through sol–gel method and used as photocatalyst. The uniformity, structure, shape, and size of the products are affected by metal salt type, fuel type, annealing temperature and time. The metal nitrate salts, sucrose, 850 ℃ and 2 h were selected as optimum precursors, fuel, annealing temperature and time, respectively. XRD indicated the successful formation of CMO/MO MCs in the presence of sucrose after annealing at 850 ℃ for 2 h. VSM showed a ferromagnetic behavior with a coercivity of 970.56 Oe. To investigation of the photocatalytic properties of CMO/MO MCs, several factors, including different organic contaminants, organic contaminant concentrations, and micro composite dosages were scrutinized to achieve the best efficiency. The photocatalytic tests indicated that micro composites can degrade RBBR in high values. For example, when 0.03 g of micro composite was used with 10 ppm RBBR under visible irradiation for 90 min, 79.18% of RBBR was destroyed. The hydroxyl radicals and holes were found to be active agents implicated in the degradation of RBBR by the scavenger's test. The recycle test unveiled that micro composites are so stable and after six cycles, the photocatalyst efficiency decreased by 12% for RBBR.

1. Introduction

Recently, oxide-based materials have received much attention as photocatalysts for water treatment. Also, the polyoxometalates and metal manganites have been the subject of much interest (Arab Fashapoyeh et al., 2018); (Mirzaei et al., 2014); (Khoshkhan et al., 2021); (Mirzaei et al., 2014); (Samaniyan et al., 2021); (Derakhshanrad et al., 2021). Polyoxometalates are discrete anionic metal–oxygen clusters, which exhibit a great diversity of sizes, nuclearities, and shapes. The mixed copper manganese oxides have a spinel structure with formula AB_2O_4. In spinel structure, B and A ions are inhabited in the octahe-

E-mail address: sobhani@kub.ac.ir
Peer review under responsibility of King Saud University.

Production and hosting by Elsevier

https://doi.org/10.1016/j.arabjc.2023.105201
1878-5352

dral and tetrahedral sites, respectively. While in inverse spinel, the A cation and half the B cations are in the octahedral and the A tetrahedral positions, respectively (Enhessari et al., 2016). $CuMn_2O_4$ is a member of the family of spinels. Copper and manganese ions in $CuMn_2O_4$, have + 2 and + 3 or + 4 and + 2 charges. This spinel is an n-type semiconductor due to electron transfers between Mn^{3+} and Mn^{2+} ions (Popescu et al., 2015). The AB_2O_4 spinels are of considerable industrial interest due to their potential applications in catalysis (Chen et al., 2016; Cheng et al., 2022; Clarke et al., 2015; Hutchings et al., 1996; Wollner et al., 1993).

$CuMn_2O_4$ structures and composites have many applications. We have devoted our efforts to synthesizing this material. $CuMn_2O_4$ has been prepared using various methods. These methods have been summarized in Table 1. In this work, $CuMn_2O_4/Mn_2O_3$ micro composites (CMO/MO MCs) are synthesized via a simple sol–gel method in the presence of sucrose for the first time. The sol–gel is a wet chemical process used to synthesize metal oxides. In this method, we can control the chemical composition of the products well because of the low reaction temperature (Bokov et al., 2021). The sol–gel is a conventional, industrial, and cost-effective method. In this method, the molecular precursor is dissolved in water or alcohol and converted to gel by heating and stirring by hydrolysis/alcoholysis. Then gel should be dried and calcined. The formation of the sol and its conversion into the gel are two basic processes in this method (Bokov et al., 2021). There is little study on the use of fuels in the sol–gel synthesis of copper manganite oxide spinels (Einaga et al., 2015; Enhessari et al., 2016; Erhardt et al., 2020). Sucrose is a low-cost and widely available compound. We used it as both fuel and chelating agent in this study (Erhardt et al., 2020). The sucrose can distribute cations homogeneously in the reaction solution. It also can accelerate combustion (Owczarz et al., 2019). Also, in this work, the photocatalytic performance of CMO/MO MCs is studied for some organic dye removal from wastewater in the presence of visible irradiation. The photocatalytic performance for the degradation of Remazol Brilliant Blue R dye (RBBR) is studied in this research, for the first time. The synthesis of micro/nanostructures is an important factor to photocatalytic water treatment. The photocatalysts has concerned a lot of consideration from scientists (Verwey and Heilmann, 1947). The photocatalytic degradation of colored pollutants in the presence of metal manganites have been studied by scientists. Larbi and co-workers investigated the photocatalytic degradation of Methylene Blue (MB) and Rhodamine B (RB) by $NiMn_2O_4$. They reported 66% and 80% decolorization efficiency for MB and RB, respectively, after 210 min (Larbi et al., 2019). Abel et al. studied Malachite Green (MG) and MB degradation in the presence of $CuMn_2O_4$ photocatalyst. They reported 92% and 86% as photocatalytic degradation percentages for MG and MB after 60 min and 120 min, respectively (Abel et al., 2019). Also, copper manganite nanostructures were synthesized and used as photocatalysts by Sobhani-Nasab. He used RB and Methyl Orange (MO) as contaminant dyes and reported 40% and 28.2% degradation in the presence of $CuMn_2O_4$ nanoparticles under UV and Vis irradiation after 70 min, respectively (Sobhani-Nasab et al., 2020). Our group has synthesized copper manganites by co-precipitation, hydrothermal and sol–gel methods and studied the photocatalytic degradation of organic dyes in the presence of copper manganites (Sobhani, 2022). Table 2 compares the photocatalytic efficiency of CMO MCs synthesized in this research with that of AMn_2O_4 spinels synthesized in the previous works. In this research, we are also studied the effect of three scavengers, including benzoquinone (BQ), benzoic acid (BA) and EDTA in the degradation of RBBR color in visible light for the first time.

Table 1 Summary of the different methods and conditions used to synthesize $CuMn_2O_4$.

Product	Synthetic method	Application	Year	Reference
$CuMn_2O_4$	Supercritical anti-solvent precipitation	Oxidation of CO	2011	(Tang et al., 2011)
$CuMn_2O_4$ supported on SiO_2	Impregnation method	Catalyst for benzene oxidation with ozone	2015	(Einaga et al., 2015)
$CuMn_2O_4$	Mechanochemical method	Oxidation of carbon monoxide	2015	(Clarke et al., 2015)
$CuMn_2O_4$	Sol-gel dip-coating	Solar absorber film	2016	(Chen et al., 2016)
$CuMn_2O_4$	Sol-gel solution combustion	To fabricate thickness-sensitive spectrally selective paint coatings	2016	(Ma et al., 2016)
$CuMn_2O_4$	Solvothermal	Electrochemical applications	2017	(Ma et al., 2016)
$CuMn_2O_4$	Reflux route	Anode for lithium-ion batteries	2018	(Saravanakumar et al., 2017)
$CuMn_2O_4$ nanoparticles and $CuMn_2O_4$-chitosan nanocomposite	Low temperature stirring technique	Sensing elements in the meters used for environmental monitoring	2019	(Li et al., 2018)
$CuMn_2O_4$	Co-precipitation	As photocatalyst for MB, MG degradation	2019	(Chani et al., 2019)
$CuMn_2O_4$	Sol-gel auto-combustion	Elimination of Hg from syngas	2020	(Abel et al., 2019)
$Cu_{1.5}Mn_{1.5}O_4$	Citric acid complexation method	Catalytic oxidation of CO	2021	(Wang et al., 2020)
CuMn2O4	Sonication	Electrod	2022	(Sun et al., 2021)
CuMn2O4/CuO nanocomposite	Hydrothermal	Photocatallyst	2022	(Sobhani, 2022)
$CuMn_2O_4/Mn_2O_3$	Sol-gel	Photothermal catalyst	2022	(Cheng et al., 2022)
CuMn2O4/Co3O4 nanocomposite	Sol-gel	photodegradation of antibiotics	2023	(Nie et al., 2022)
CuMn2O4/CeO2 nanocomposites	Sol-gel	Photocatalyst for the H_2 evolution	2023	(Almenia et al., 2023)
CuMn2O4 on graphene sheets	Reflux	Electrode	2023	(Alzahrani et al., 2023)
CuMn2O4/chitosan micro/nanocomposite	Hydrothermal	MB removal	2023	(Nikhil Chandran et al., 2023; Samadi Kazemi and Sobhani, 2023)

Table 2 The comparison of the photocatalytic efficiency of CMO MCs synthesized in this research with that of AMn_2O_4 spinels synthesized in the previous works.

Photocatalyst	Organic dye	Irradiation Time(min)	Degradation%	Reference
$CuMn_2O_4/Mn_2O_3$ microcomposites	Remazol Brilliant Blue R	90	79	Present work
$CuMn_2O_4$	Rhodamine B	60	68	(Salunkhe et al., 2012)
	Methyl Orange	60	38	
$CuMn_2O_4$	Malachite Green	60	92	(Pedra et al., 2016)
	Methylene Blue	120	86	
$CuMn_2O_4/CuO$ nanocomposites	Malachite Green	90	73 (under vis)	(Samaniyan et al., 2021)
$CuMn_2O_4$ nanoparticles	Rhodamine B	70	76 (under UV)	(Salunkhe et al., 2012)
	Rhodamine B	70	45.2 (under vis)	
$CuMn_2O_4$ nanoparticles	Methyl Orange	70	40 (under UV)	(Salunkhe et al., 2012)
	Methyl Orange	70	28.2 (under vis)	
$NiMn_2O_4$	Methylene Blue	210	66	(Bhagwat et al., 2019)
	Rhodamine B	210	80	

2. Experimental

2.1. Materials and experiments

Materials used in this work are $Cu(NO_3)_2{\cdot}3H_2O$, $Mn(NO_3)_2{\cdot}4H_2O$, and sucrose. These materials were purchased from Merck company. A Philips X′pertPro X-ray diffractometer with Ni-filtered Cu Kα radiation and λ = 1.54 Å was used to obtaine XRD patterns. A TESCAN Mira3 field emission scanning electron microscope (FE-SEM) was used to investigate the morphology of the products. This microscope was also used to study energy dispersive X-ray spectrum (EDS). A Nicolet IS 10 spectrophotometer of American Thermo scientific company was used to take Fourier Transform Infrared (FT-IR) spectrum. A vibrating sample magnetometer (VSM) of Meghnatis Kavir Kashan was used to study the magnetic property of the products.

2.2. Synthesis of $CuMn_2O_4/Mn_2O_3$ micro composites

$CuMn_2O_4/Mn_2O_3$ micro composites were prepared via sol–gel method. First an aqueous solution of $Cu(NO_3)_2{\cdot}3H_2O$ (concentration 0.024 M) was prepared. Then a sucrose solution with concentration 0.144 M was added into it. After stirring for 30 min, the $Mn(NO_3)_2{\cdot}4H_2O$ solution (concentration 0.048 M) was added into the solution under stirring. The stoichiometric ratio of Cu:Mn:sucrose was selected to be 1:2:6. The solution was stirred at 100 ℃ for 60 min. Evaporation of the mixed solution caused formation of a highly viscous gel. The gel then is dried in an oven at 200 ℃. The final residue is annealed in furnace at different temperatures (500 ℃, 700 ℃ and 850 ℃) for 2 h to examine the effect of high temperature exposure on the micro composite. The micro composite is maintained in penicillin vial and characterized by XRD, SEM, VSM, FT-IR and EDS. Table 3 shows the reaction conditions for the synthesis of CMO/MO MCs in this work. Scheme 1 is a diagram illustrating the synthesis and characterization of CMO/MO MCs.

2.3. Photocatalytic measurements

For the investigation of the photocatalytic activity of the micro composites, RBBR and MG were applied as two contaminant anionic and cationic dyes. The specified quantities of the

Table 3 The reaction conditions for the synthesis of CMO/MO MCs in this work.

Sample	Cu Source	Mn Source	Fuel	Cu:Mn: Fuel	Annealing Temperature(C)	Annealing Time (h)	Product
1	$Cu(NO_3)_2{\cdot}3H_2O$	$Mn(NO_3)_2{\cdot}4H_2O$	Sucrose	1:2:6	850	2	Polygonal microprisms of $CuMn_2O_4/Mn_2O_3$
2	$Cu(NO_3)_2{\cdot}3H_2O$	$Mn(NO_3)_2{\cdot}4H_2O$	Sucrose	1:2:6	700	2	Cu
3	$Cu(NO_3)_2{\cdot}3H_2O$	$Mn(NO_3)_2{\cdot}4H_2O$	Sucrose	1:2:6	500	2	Cu
4	$Cu(NO_3)_2{\cdot}3H_2O$	$Mn(NO_3)_2{\cdot}4H_2O$	Sucrose	1:2:6	850	4	Spherical nanostructures
5	$Cu(NO_3)_2{\cdot}3H_2O$	$Mn(NO_3)_2{\cdot}4H_2O$	Glucose	1:2:6	850	4	Microspheres
6	$Cu(NO_3)_2{\cdot}3H_2O$	$Mn(NO_3)_2{\cdot}4H_2O$	Fructose	1:2:6	850	4	Microspheres
7	$Cu(NO_3)_2{\cdot}3H_2O$	$Mn(NO_3)_2{\cdot}4H_2O$	Maltose	1:2:6	850	4	Agglomerated nanoparticles
8	$CuCl_2$	$Mn(NO_3)_2{\cdot}4H_2O$	Glucose	1:2:6	850	4	Microspheres

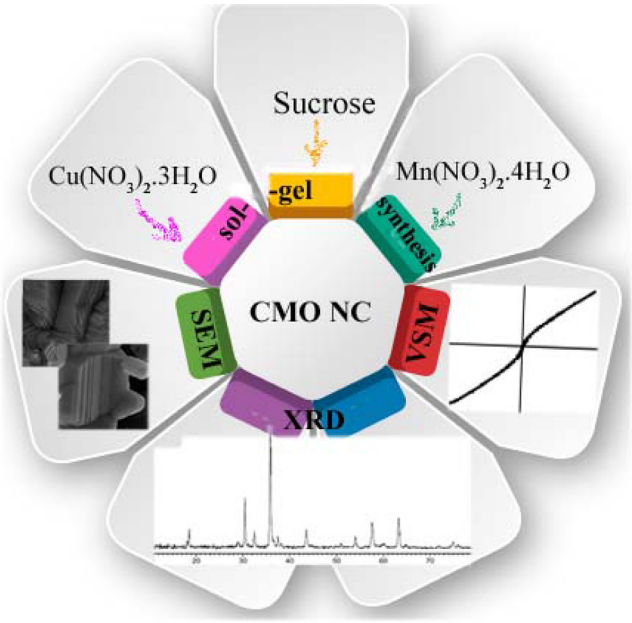

Scheme 1 Diagram illustrating the synthesis and characterization of CMO/MO MCs.

CMO/MO MCs were weighted and used for the degradation of dye solutions with different concentrations. The micro composites were suspended in 30 mL of the dye solution in a quartz reactor. The suspension was aerated in darkness and was stirred constantly for 15 min. It was placed under visible irradiation by an Osram 400 W visible light (containing a wavelength in the range of 400 to 780 nm) at a space of 40 cm away from it. Then suspension containing dye was aerated continuously to supply O_2. After 10 min stirring under visible irradiation, 5 mL of the suspension was sampled. In order to ensure removing the photocatalyst from samples, the suspension was centrifuged and scrutinized with a UV–Vis spectrometer and its absorbance spectrum was recorded. We used the below equation to estimate the photocatalytic degradation of the dyes:

$$Degradation\% = [\frac{A_0 - A}{A_0}] \times 100 \quad (1)$$

A_0 and A in above equation are absorbance quantities of dye solution before and after decomposition, respectively (Mahdiani et al., 2019). To optimize the photocatalytic activities, three effects including type and concentration of dye, and photocatalyst dose were studied in this work.

3. Results and discussion

3.1. Phase purity and chemical structure

XRD analyzed the crystalline structures of powders synthesized by sol–gel. Fig. 1 shows the XRD results of samples 1, 2 and 3. The formation of $CuMn_2O_4$ is confirmed in sample 1 through XRD. Also, a small percentage of the secondary phase of Mn_2O_3 is observed in this sample. In Fig. 1a, the 2θ values at 30.43°, 35.84°, 57.59° and 63.27° correspond to (*hkl*) planes (220), (311), (511) and (440) of $CuMn_2O_4$ (with JCPDS card no. 01–084-0543), respectively. The prepared $CuMn_2O_4$ has Fd-3 m space group and face centered cubic structure. Also, Scherer formula (Eq. (2) was used to calculate the average crystallite size of $CuMn_2O_4$ (Sobhani, 2022):

$$D = \frac{K\lambda}{\beta cos\theta} \quad (2)$$

In this equation, D, K, λ, β, θ are average crystallite size, dimensionless shape factor, X-ray wavelength, line broadening at half the maximum intensity (FWHM), and Bragg angle, respectively. K value is about 0.9 and varies with the shape of the crystallites. D was calculated 34.00 nm for sample 1. In the XRD patterns of samples 2 and 3, the $CuMn_2O_4$ is not present, and as shown in Fig. 1b and c after annealing at 700 ℃ and 500 ℃ a single Cu phase is formed. Thus, the successful sol–gel synthesis of copper manganites is achieved when using sucrose as fuel and 850 ℃ as annealing temperature.

3.2. Microscopic structure

SEM and TEM images in Fig. 2 show the morphology of the copper manganites prepared via the sol–gel method at 850 ℃ (sample 1). SEM images in Fig. 2a-d show the formation of polygonal micro prisms stuck together. TEM images in Fig. 2e, f show that the diameters of the base of these prisms are 300–700 nm. As the baking process continues to 4 h, the prisms destroy, and spherical nanostructures form, as shown in SEM images in Fig. 3. It seems that all samples have a high tendency towards spherical morphology.

We continued the sol–gel method to synthesize copper manganites in the presence of different fuels, including glucose, fructose, and maltose. SEM images in Fig. 4 show that microspheres form in the presence of glucose and fructose, as two monosaccharides. Fig. 4a and b show that the microspheres with diameters 50 nm-1 μm form in the presence of glucose. The surfaces of the spheres have been covered with nanoparticles. These microspheres are probably formed from the accumulation of nanoparticles. The products prepared with fructose (sample 4) are microspheres with diameters 2–5 μm, also nanoparticles with diameters of about 70 nm form in the presence of this fuel (as shown in Fig. 4c and d). The use monosacarides can lead to decreased formation of nucleation points. The lower number of these points for crystal growth translates into increased growth of the created nuclei, resulting in larger particles. Agglomerated nanoparticles with diameters $\leq$ 100 nm formed when using maltose as fuel, as shown in Fig. 4e, f. Also, dense agglomerates of nanoparticles are observed in this figure that construct nanospheres. The morphology of samples 2 and 5 are similar. Both samples 2 and 5 have synthesized in the presence of disacarides. The decrease in particle size in samples prepared with disacarides than that prepared with monosacarides is observed clearly in SEM images in Figs. 3 and 4. This decrease highlights the influence of sucrose and maltose on the particle size of the crystallites. SEM results show that in this work conditions, disaccharides are suitable fuels for so-gel synthesis of manganites.

In continuation, the effect of the copper salt on the morphology of the manganites studies. SEM images in Fig. 5 are related to the sample prepared from $CuCl_2$ and $Mn(NO_3)_2{\cdot}4H_2O$ in the presence of glucose (sample 6). Changing the cop-

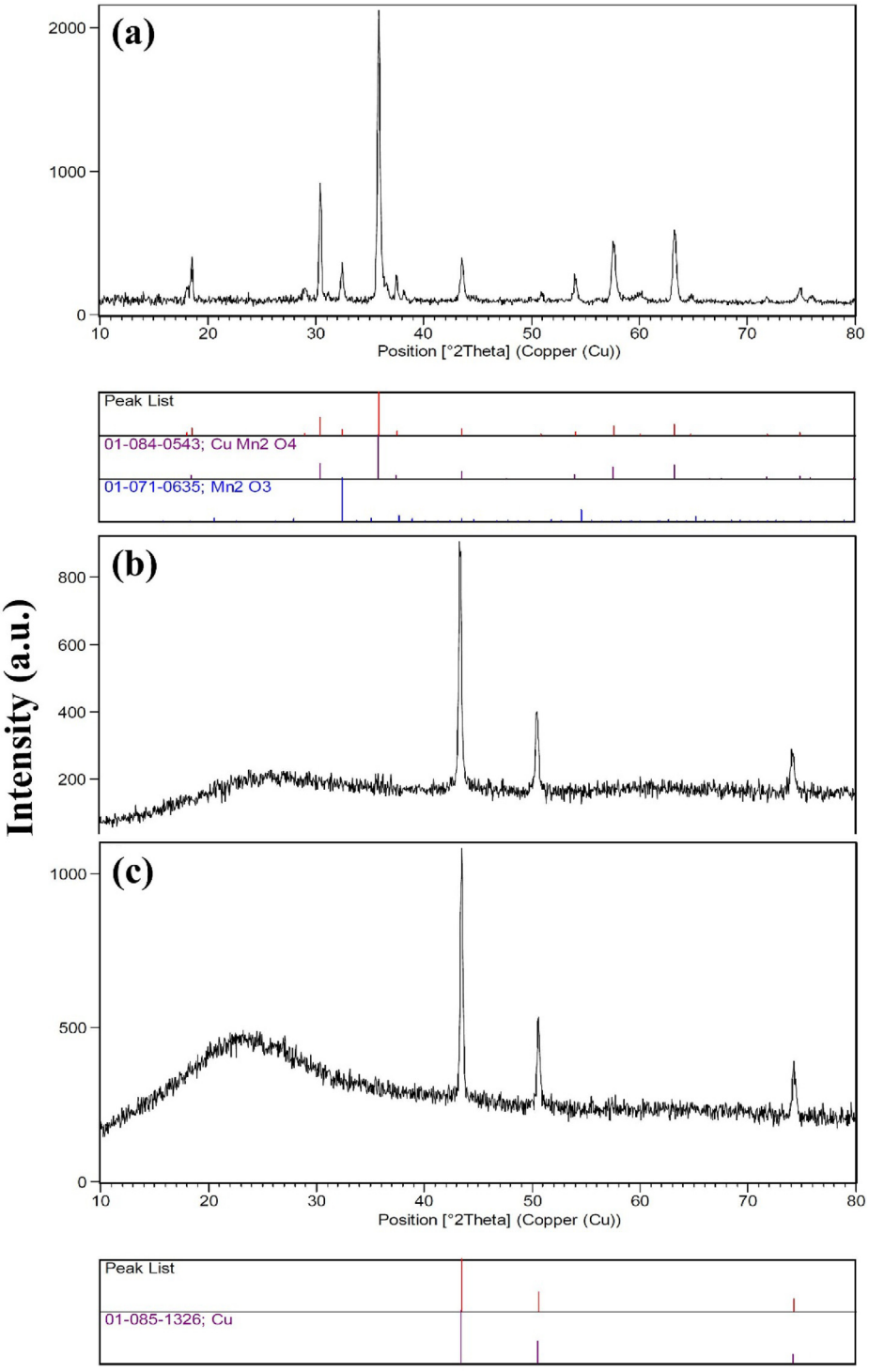

Fig. 1 XRD patterns of the products prepared from Cu and Mn nitrate salts in the presence of sucrose via sol–gel method at different annealing temperatures for 2 h: (a) 850 ℃ (sample 1), (b) 700 ℃ (sample 2) and (c) 500 ℃ (sample 3).

per salt, the morphology of the composites does not change. Both samples as-prepared from nitrate and chloride copper salts are microspheres with none-even diameters. The surfaces of microspheres in both samples have been covered with nanoparticles. The microspheres in sample 6 have larger diameters than that of sample 3. These different diameters can be due to the difference in release rates of Cu^{2+} ions from their salts. Under the same conditions, the particle size decreases by decreasing the release rate of Cu^{2+} from its salts.

3.3. EDS, FT-IR spectra

EDS is an elemental spectroscopy technique, which goes hand in hand with electron microscopy. Fig. 6 shows EDS spectrum

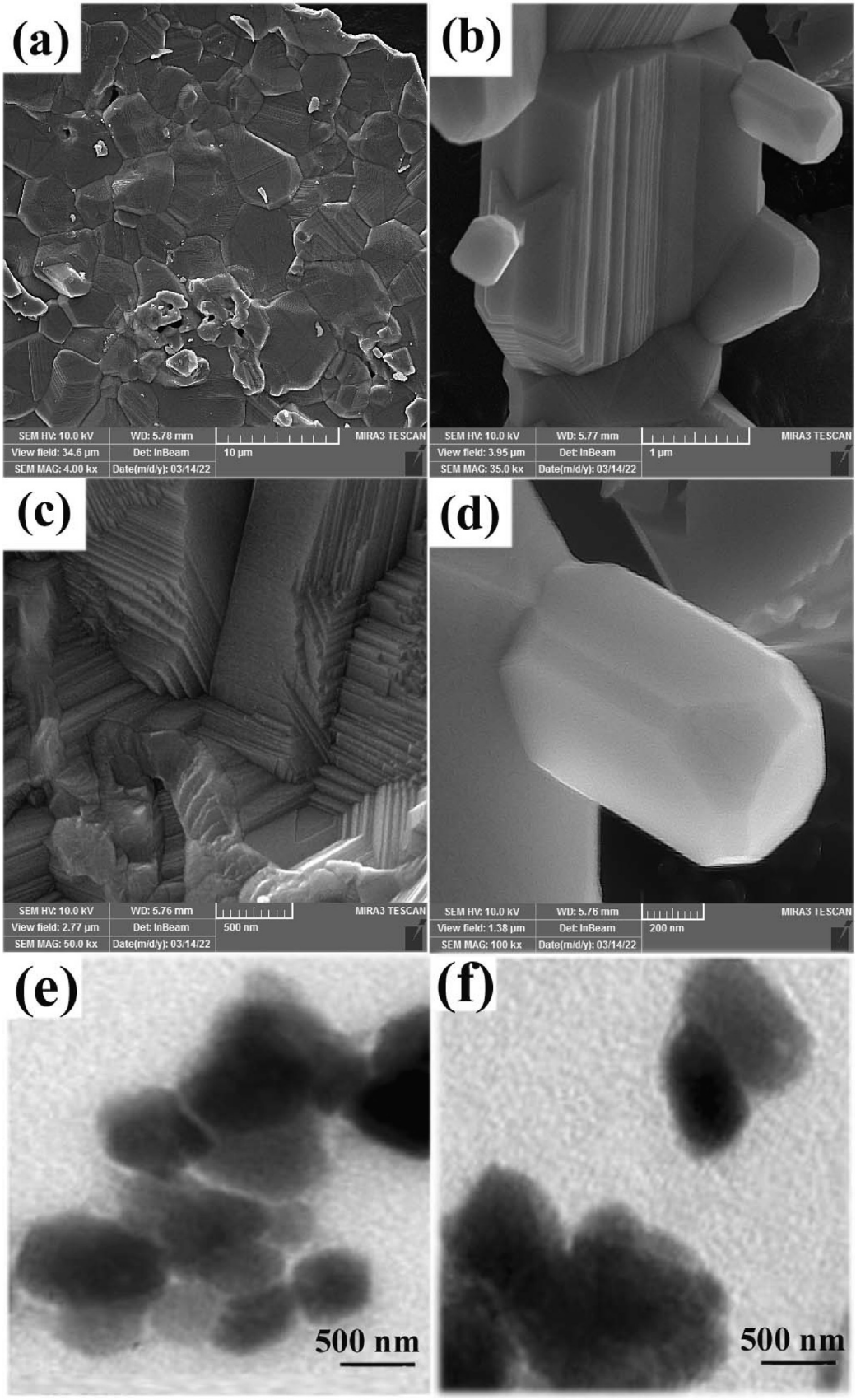

Fig. 2 (a-d) SEM and (e, f) TEM images of the product prepared from Cu and Mn nitrate salts in the presence of sucrose via sol–gel method after annealing at 850 ℃ for 2 h (sample 1).

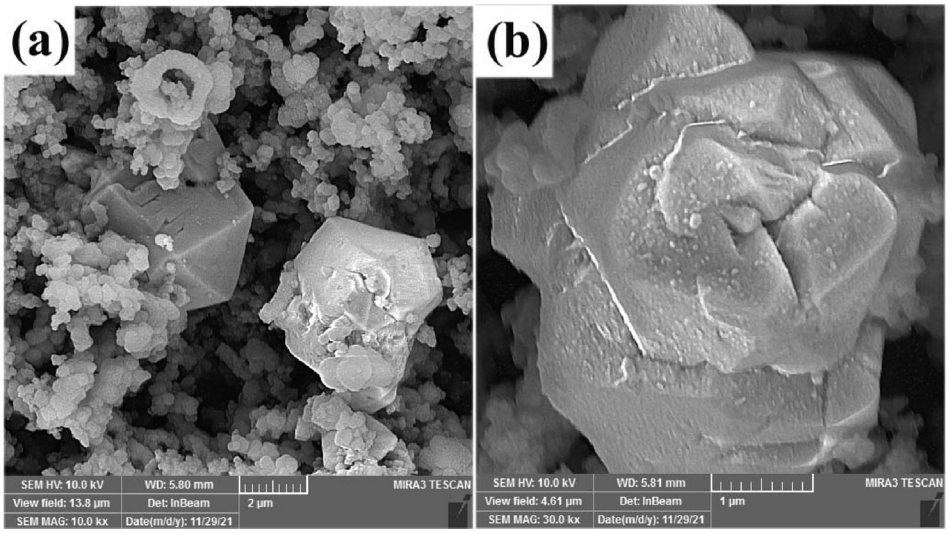

Fig. 3 SEM images of the product prepared from Cu and Mn nitrate salts in the presence of sucrose via sol–gel method after annealing at 850 ℃ for 4 h (sample 4).

of CMO/MO NCs (sample 1) and confirms the presence of Cu, Mn and O elements in chemical composition of this sample. According to this figure, the atomic percentages of Cu, Mn and O are 10.99 %, 21.60 % and 67.41 %, respectively. The results obtained from EDS spectrum confirm the XRD results in Fig. 1a and also formation of CMO/MO NCs.

Fig. 6b shows FT-IR spectrum of sample prepared from Cu and Mn salts in the presence of sucrose via sol–gel method (sample 1). This spectrum has been recorded between 4000 and 500 cm^{-1}. The emission, absorption and photoconductivity of gas, liquid, and solid can be obtain by FT-IR technique. This spectrum identifies different functional groups in sample. The magnitude and symmetry of the dipole moment of the bonds in the sample are effective agents in the intensity of the FT-IR peaks. In Fig. 6b the low-intensity and broad peak at about 3250 cm^{-1} shows water absorption on the surface of the sample 1. This region is related to O–H stretching vibrations. The peaks at 1557.75 and 1361.80 cm^{-1} correspond to H_2O bending vibrations and organic residues in the product, respectively. The absorption bond in the area of the 598.46 cm^{-1} is attributed to manganese-oxygen lattice vibrations. This high-intensity and low-frequency mode in FT-IR spectrum of sample 1 is related to the stretching vibrations of Mn-O bond (Abel et al., 2019); (Wang et al., 2013) . FT–IR results for sample 1 confirm the formation of CuMnO nanostructures.

3.4. Magnetic and optical studies

VSM is one of the most successful implementations of a magnetometer. It is a versatile technique for measuring the magnetic moment of a sample when it is vibrated perpendicularly to a uniform magnetizing field. Changes as small as 10^{-5} to 10^{-6} emu can be detected with this method. Fig. 7 shows magnetization curve of sample 1 measured using VSM, which gives the magnetic moment of the sample as a function of applied magnetic field. The figure shows a ferromagnetic behavior with a coercivity of 970.56 Oe in low fields. Also, Fig. 7 shows an antiferromagnetic behavior for the micro composites in high fields. It is due to the contribution of super-exchange interactions between Mn ions (Mn^{3+}–O^{2-}–Mn^{4+}).

Fig. 8a shows UV–Vis DRS absorption spectrum of sample 1 between 200 and 700 nm. A sharp absorbance peak at about 246 nm is seen in this figure. This peak is due to the creation of electron-hole recombination on the surface of CMO MCs.

3.5. Photocatalytic studies

In this work, two dyes including RBBR and MG were used in order to investigation of the effect of anionic and cationic dyes. As shown in Fig. 8b, the photocatalytic performance of CMO/MO MCs is higher for the degradation of RBBR anionic dye than that for the degradation of MG cationic dye. The RBBR is an anionic contaminant and its oxygen groups can increase electron density on surfaces of the photocatalyst. Thus, in the present work condition, photocatalytic activity of the as-prepared composite is higher for the RBBR degradation than MG. The degradations were reported 79.17% and 21.01% in the presence of CMO/MO MCs, after 90 min visible light irradiation, for EBBR and MG, respectively.

The as-prepared CMO/MO MCs in this work were used as photocatalyst for RBBR degradation. Fig. 9a shows effect of the amount of composite on the RBBR degradation percent. Increasing the photocatalyst amount, RBBR degradation increased because the dye interaction with the photocatalyst increased. Also, this increase was because of increasing local active sites to adsorb dye molecules. The more increasing photocatalyst at constant RBBR concentration and volume, the opposite result was obtained. RBBR degradation decreased with a more increase in the amount of photocatalyst, due to these reasons: (1) aggregation resulting from high photocatalyst dose, (2) decrease in total surface area of the photocatalyst, (3) increase in diffusional path length, (4) unsaturation of photocatalyst sites through the adsorption process. The degradation percent of 10 ppm solution of RBBR in the presence of 0.02, 0.03, and 0.05 g photocatalyst was measured 31.91 %, 79.17 %, and 60.94 % after 90 min visible irradiation, respectively.

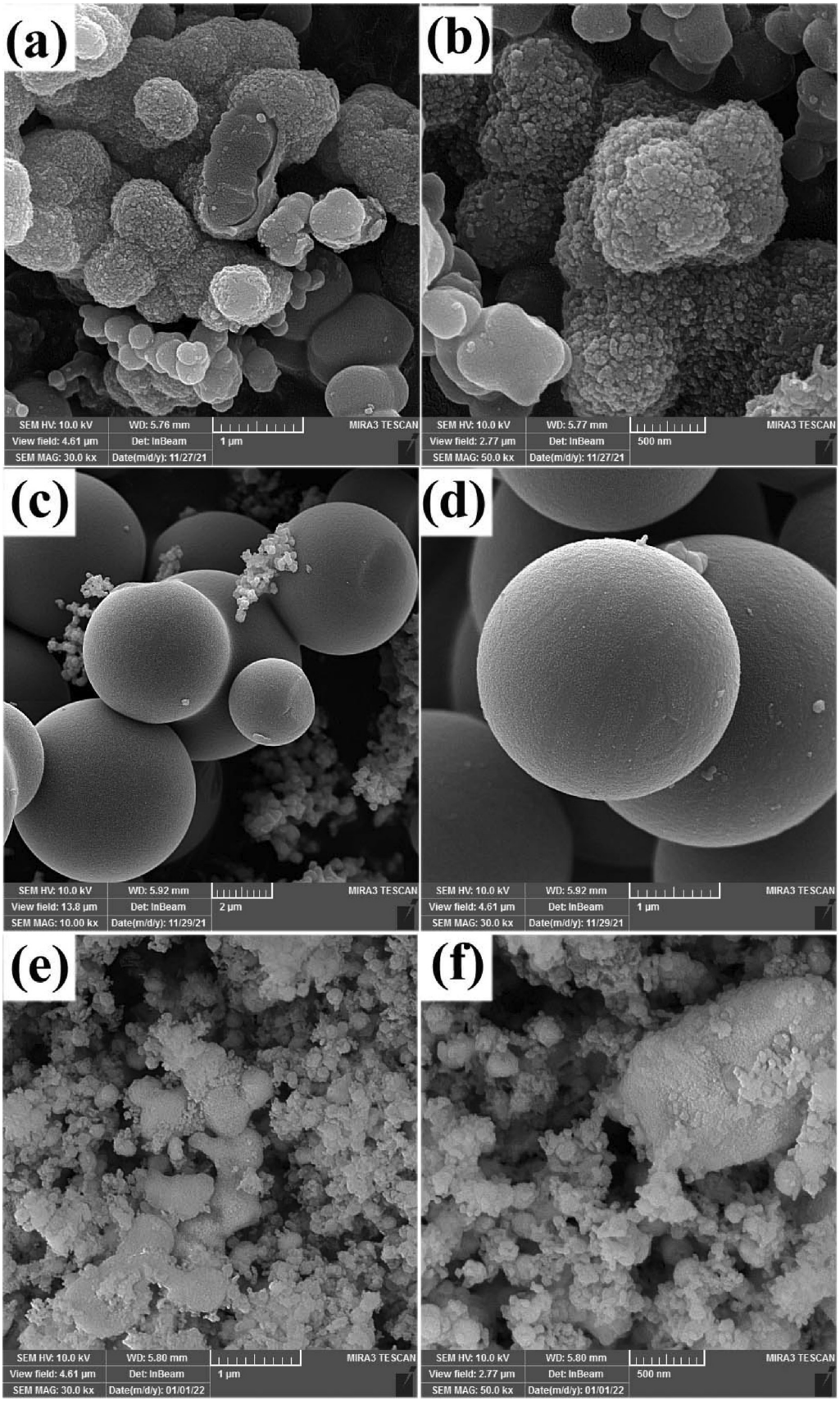

Fig. 4 SEM images of the products prepared from Cu and Mn nitrate salts in the presence of different fuels via sol–gel method at 850 ℃ for 4 h: (a, b) glucose (sample 5), (c, d) fructose (sample 6) and (e, f) maltose (sample 7).

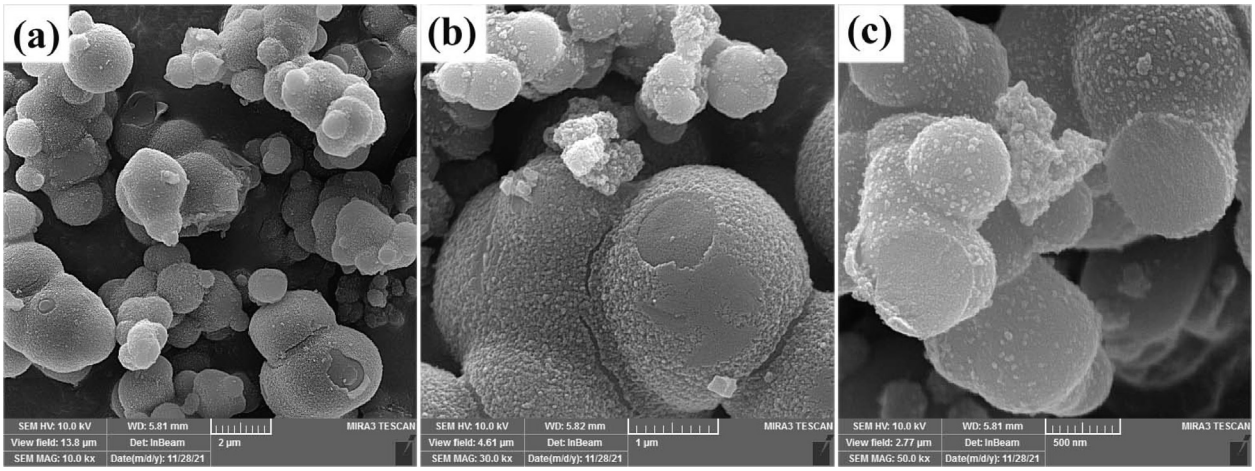

Fig. 5 SEM images of the product prepared from $CuCl_2$ and $Mn(NO_3)_2{\cdot}4H_2O$ in the presence of glucose via sol–gel method at 850 ℃ for 4 h (sample 8).

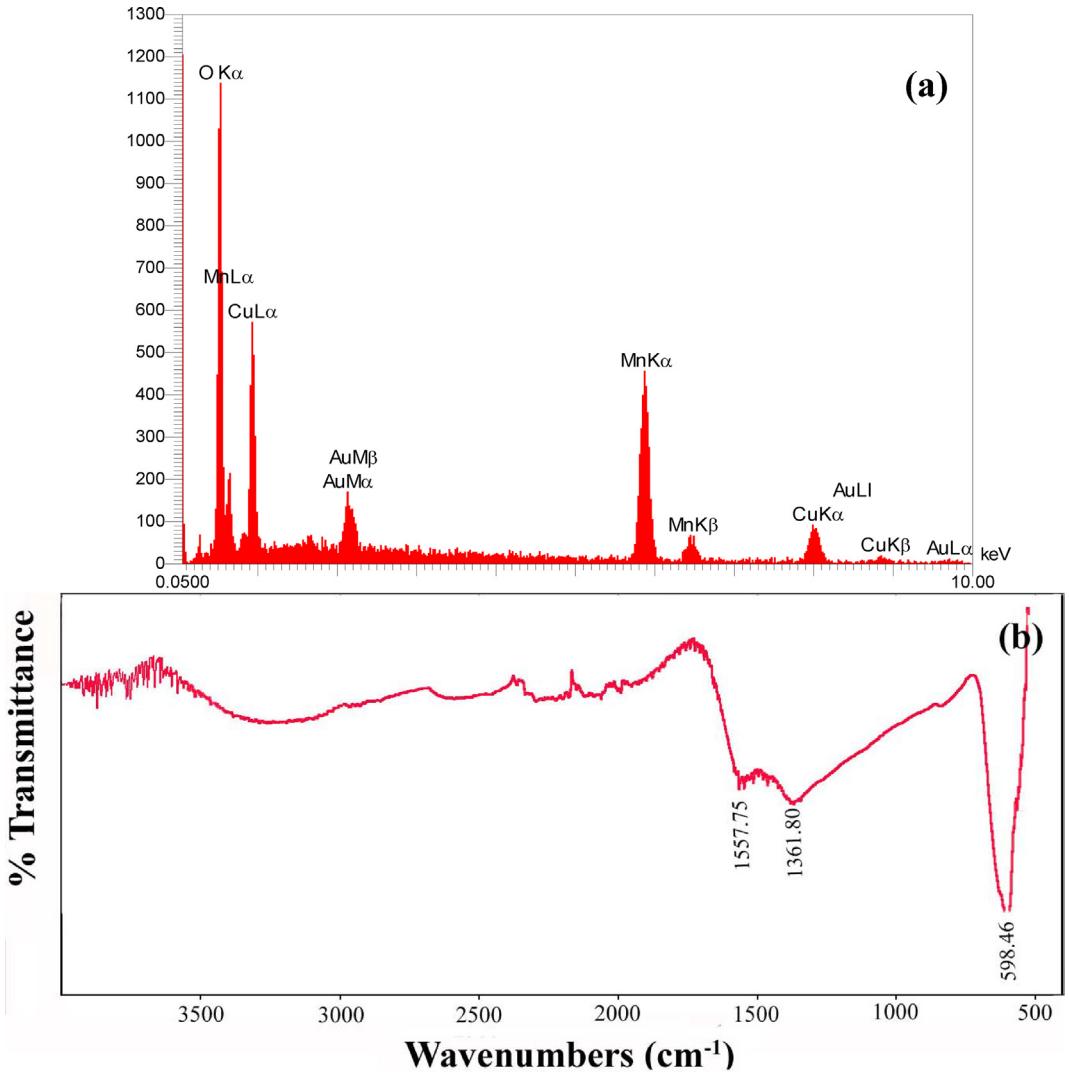

Fig. 6 (a) EDS and (b) FT-IR spectra of the product prepared from Cu and Mn salts in the presence of sucrose via sol–gel method at 850 ℃ for 2 h (sample 1).

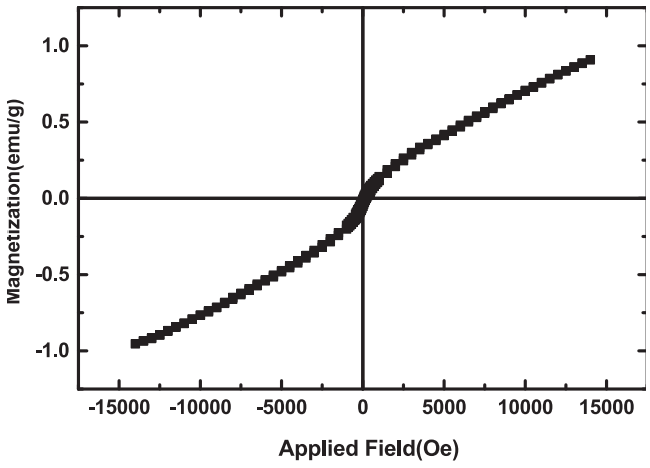

Fig. 7 Magnetization curve versus field of the product prepared from Cu and Mn salts in the presence of sucrose via sol–gel method at 850 ℃ for 2 h (sample 1).

In order to investigation of effect of dye concentration on the photocatalytic activity of CMO/MO MCs, three RBBR solutions with 5, 10 and 15 ppm concentrations were prepared. The photocatalytic tests were investigated and results have shown in Fig. 9b. The figure shows that with the increase in RBBR concentration (from 10 to 15 ppm) its degradation percentage decreases. The degradation percentage for a 10 ppm solution of RBBR was obtained 79.17% after 90 min of irradiation. This percentage was decreased to 69.23 % for a 15 ppm solution of RBBR. Increasing dye concentration and thus increasing number of dye molecules, these molecules can compete with the generated oxidizing agents to adsorb on the surface of the photocatalyst. This competition can slow the degradation process by reducing number of available oxidant agents in the solution. Also, in the high dye concentrations, the production of electron and hole is lowered because of the lowering of light penetrating power that can lower rate of photodegradation. In this study we found an interestingly result.

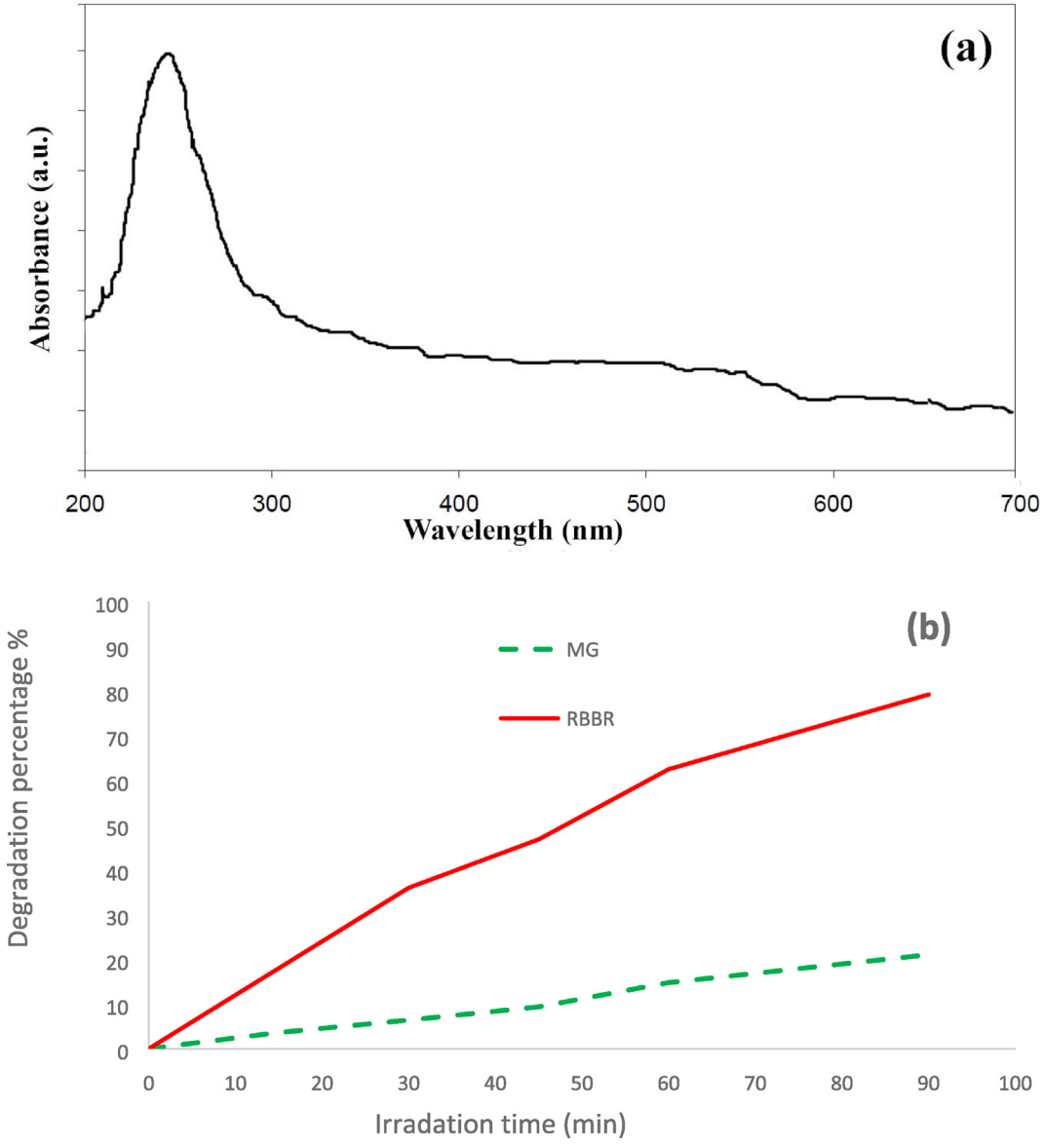

Fig. 8 (a) UV–Vis DRS absorption spectrum of sample 1, (b) Photocatalytic activity of sample 1 for degradation of RBBR and MG under visible light irradiation.

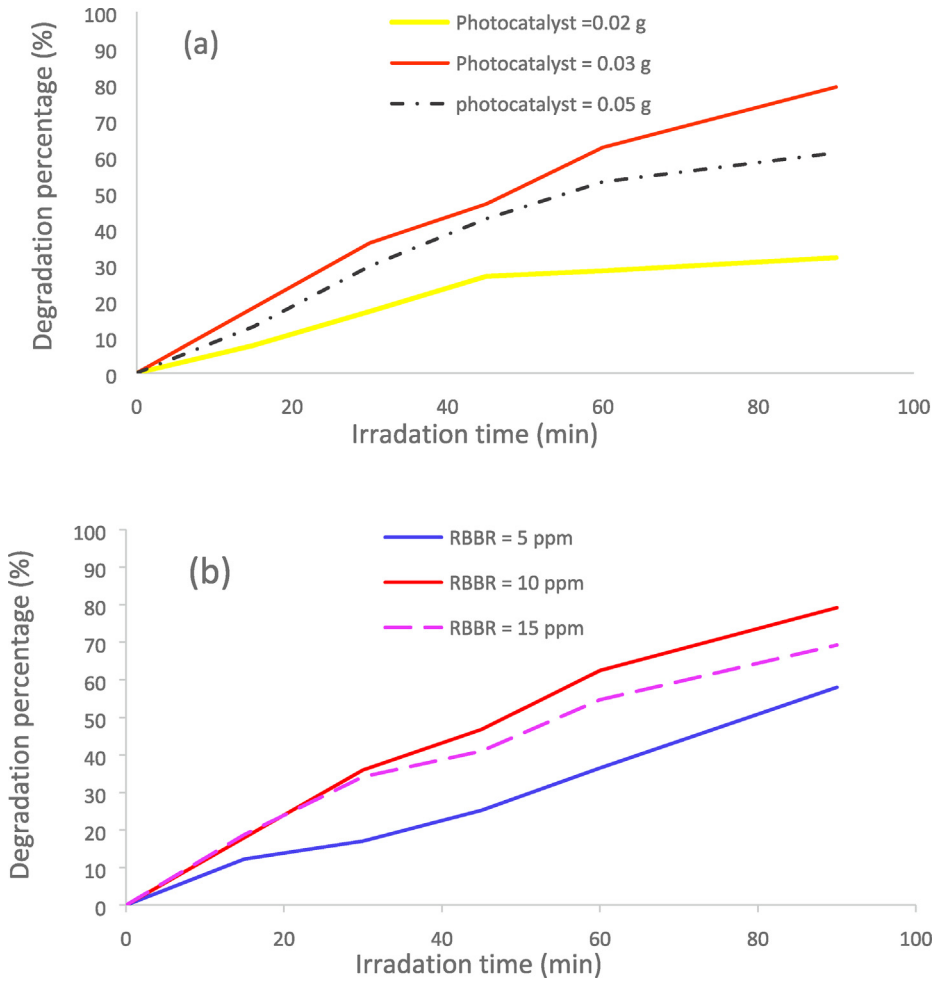

Fig. 9 Investigation of the effects of: (a) photocatalyst dose and (b) dye concentration on the RBBR degradation under visible irradiation.

The photocatalytic tests done for the investigation of the effect of dye concentration showed a deflection at 5 ppm solution of RBBR. The degradation percentage was decreased to about 58% for 5 ppm solution of RBBR. The optimum conditions for the photocatalytic degradation in this synthesis were selected: RBBR solution with 10 ppm concentration and 0.03 g CMO/MO MCs as photocatalyst.

The photocatalytic activity mechanism of the nanocomposites for RBBR degradation proposes as follows. The RBBR is excited using visible irradiation, and the electrons of its valance band are moved to the conduction band of CMO NC. Then, these electrons are borrowed by the oxygens present in the water. Then oxygen radicals, which are reactive species, are produced. The removal of pollutants is done by active spices, for example hole, radical, and anion of superoxide (Mahdiani et al., 2017, 2019, Mirzaei et al., 2014a,b; Mohassel et al., 2018a,b). The pairs of electron–holes create owing to the excitation of CMO under visible irradiation, which delivers the required circumstances to create reactive oxygen species leading to pollutant removal (Jeyasubramanian et al., 2015). The below equations are several reaction sequences and suggest the photocatalytic degradation of the RBBR in this study:

$$CMO \rightarrow CMO\left(e_{CB}^{-} + h_{VB}^{+}\right) \quad (3)$$

$$CMO\left(h_{VB}^{+}\right) + H_2O \rightarrow CMO + H^{+} + OH^{o} \quad (4)$$

$$CMO\left(e_{CB}^{-}\right) + O_2 \rightarrow CMO + O_2^{0-} \quad (5)$$

$$O_2^{0-} + H^{+} \rightarrow HO_2^{0} \quad (6)$$

$$RBBR + OH^{0} \rightarrow \text{degradated RBBR} \quad (7)$$

$$RBBR + h_{VB}^{+} \rightarrow \text{oxidation} \quad (8)$$

$$RBBR + e_{CB}^{-} \rightarrow \text{reduction} \quad (9)$$

The active species were scrutinized to comprehend the mechanism of the photocatalytic process. The most likely active species implicated in the photodegradation of organic pollutants are superoxide radical anions (O_2^{0-}), hydroxyl radicals (OH^0), and holes (h^+). These active species are called scavengers. A scavenger is a chemical substance added to a mixture in order to remove or de-activate impurities and unwanted reaction products. Three scavenger species, BQ, BA, and EDTA as scavengers of O_2^{0-}, OH^0 , and h^+ were studied to determine which active species are more in charge of the degradation of RBBR in the photocatalytic reaction (Zhang et al., 1998). The degradation percentage of RBBR in the presence

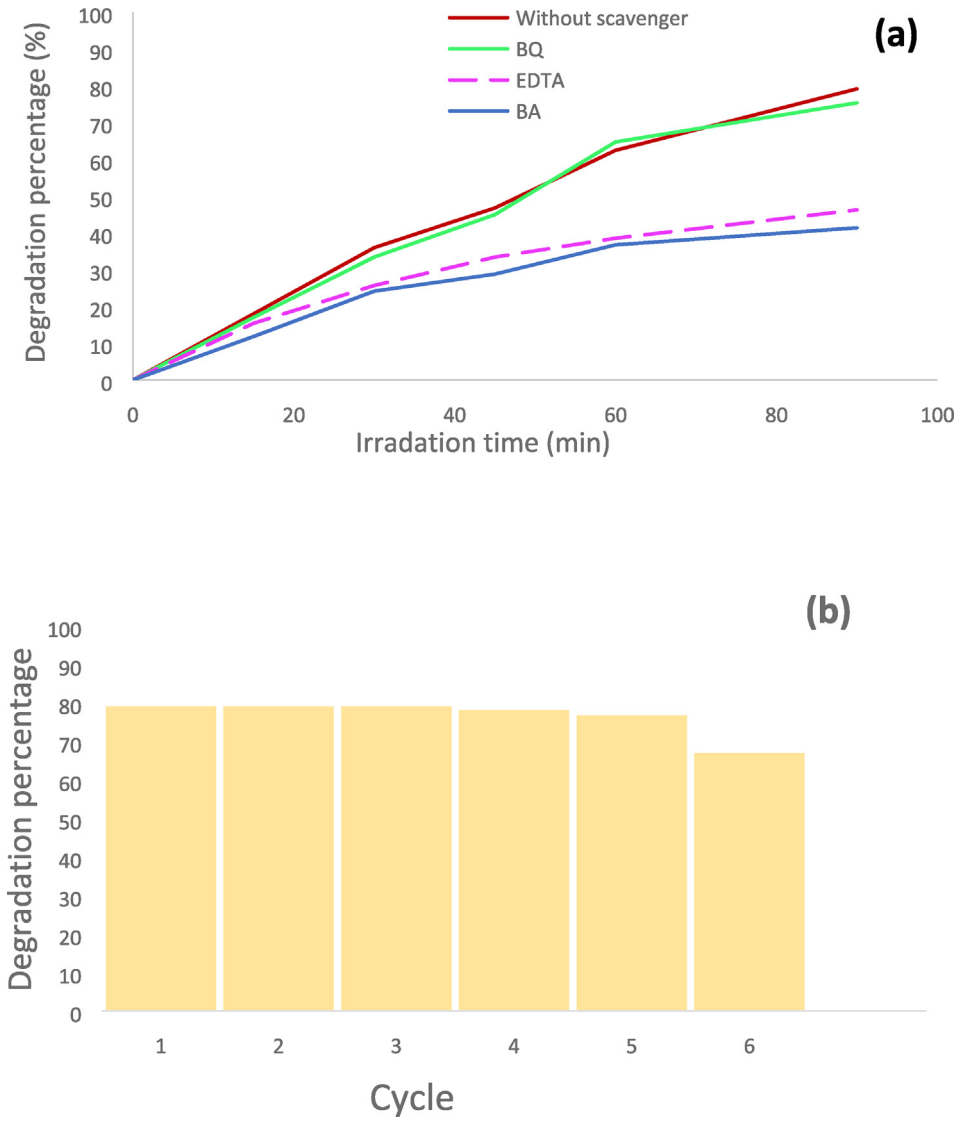

Fig. 10 (a) The mechanism study using scavengers for RBBR degradation under visible irradiation, (b) Recycling tests of sample 1 for RBBR degradation under visible light irradiation.

of these scavengers has been reported in Fig. 10a. As shown in this figure, the degradation efficiency has decreased in the presence of BA and EDTA. This decrease shows the role of hydroxyl radical and holes in the photocatalytic removal of RBBR (Ryu and Choi, 2006). Also, the stability of sample 1 as photocatalyst was investigated and destruction reactions were repeated (6 cycles). The degradation percentages were reported 79.18 %, 79.18 %, 79.18 %, 78.24 %, 76.84 %, and 67 % after six cycles for the photocatalyst toward the RBBR, as shown in Fig. 10b. We observed an activity loss about 12 % after six consecutive reactions due to the high stability of the CMO/MO MCs synthesized in this work.

4. Conclusions

CMO/MO MCs with a ferromagnetic behavior were prepared using the sol–gel method. The effects of metal salt type, fuel type, annealing temperature and time were investigated on the uniformity, shape, structure, size, and purity of the microcomposites. The sucrose was selected as optimum fuel. The photocatalytic behavior of CMO/MO MC showed that this compound has high potential in the degradation of RBBR. The studies indicated that 0.03 g microcomposite can degrade 79.18% of 10 ppm RBBR under visible light after 90 min. To highlight the photostability of CMO/MO MCs, we studied six cycles toward the RBBR and observed a low activity loss due to the high stability of the micro composites. The scavenger experiments indicated that hydroxyl radicals and holes perform roles in the photocatalysis process.

Declaration of Competing Interest

The authors declare that they have no known competing financial interests or personal relationships that could have appeared to influence the work reported in this paper.

Acknowledgment

The study was supported by Kosar University of Bojnord with the grant number (NO. 0110201612).

References

M.J. Abel, A. Pramothkumar, N. Senthilkumar, K. Jothivenkatachalam, P.F.H. Inbaraj, J.J. Prince, Flake-like $CuMn_2O_4$ nanoparticles synthesized via co-precipitation method for photocatalytic activity, *Phys. B (Amsterdam, Neth.)* 572 (2019) 117-124.

Abel, M.J., Pramothkumar, A., Senthilkumar, N., Jothivenkatachalam, K., Inbaraj, P.F.H., Prince, J.J., 2019. Flake-like $CuMn_2O_4$ nanoparticles synthesized via co-precipitation method for photocatalytic activity. J. Phys. B 572, 117–124.

Almenia, S.H., Ismail, A.A., Alzahrani, K.A., Aljahdali, M., 2023. Fabrication of $CuMn_2O_4/Co_3O_4$ nanocomposite heterojunctions for efficacious visible light-induced degradation of antibiotics. Ceram. Int. 49, 13227–13237.

Alzahrani, K.A., Ismail, A.A., Alahmadi, N., 2023. Heterojunction of CuMn2O4/CeO2 nanocomposites for promoted photocatalytic H2 evolution under visible light. J. Taiwan Inst. Chem. Eng. 143, 104692.

Arab Fashapoyeh, M., Mirzaei, M., Eshtiagh-Hosseini, H., Rajagopal, A., Lechner, M., Liu, R., Streb, C., 2018. Photochemical and electrochemical hydrogen evolution reactivity of lanthanide-functionalized polyoxotungstates. Chem. Commun. 54, 10427–10430.

Bhagwat, V.R., Humbe, A.V., More, S.D., Jadhav, K.M., 2019. Sol-gel auto combustion synthesis and characterizations of cobalt ferrite nanoparticles: different fuels approach. Mater. Sci. Eng. B 248, 114388.

Bokov, D., Jalil, A.T., Chupradit, S., Suksatan, W., Ansari, M.J., Shewael, I.H., Valiev, G.H., Kianfar, E., 2021. Nanomaterial by Sol-Gel Method: Synthesis and Application. Adv. Mater. Sci. Eng. 2021, 1–21.

Chani, M.T.S., Karimov, K.S., BahadarKhan, S., Fatima, N., Asiri, A.M., 2019. Impedimetric humidity and temperature sensing properties of chitosan-$CuMn_2O_4$ spinel nanocomposite. Ceram. Int. 45, 10565–10571.

Chen, H., Zhou, M., Wang, T., Li, F., Zhang, Y.X., 2016. Construction of unique cupric oxide–manganese dioxide core–shell arrays on a copper grid for high-performance supercapacitors. J. Mater. Chem. A 4, 10786–10793.

Cheng, C., Cheng, Y., Lai, G., 2022. $CuMn_2O_4$ hierarchical microspheres as remarkable electrode of supercapacitors. Mater. Lett. 317, 132102.

Clarke, T.J., Davies, T.E., Kondrat, S.A., Taylor, S.H., 2015. Mechanochemical synthesis of copper manganese oxide for the ambient temperature oxidation of carbon monoxide. Appl Catal B 165, 222–231.

Derakhshanrad, S., Mirzaei, M., Streb, C., Amiri, A., Ritchie, C., 2021. Polyoxometalate-based frameworks as adsorbents for drug of abuse extraction from hair samples. Inorg. Chem. 60, 1472–1479.

Einaga, H., Maeda, N., Yamamoto, S., Teraoka, Y., 2015. Catalytic properties of copper-manganese mixed oxides supported on SiO_2 for benzene oxidation with ozone. Catal. Today 245, 22–27.

Enhessari, M., Salehabadi, A., Maarofian, K., Khanahmadzadeh, S., 2016. Synthesis and physicochemical properties of $CuMn_2O_4$ nanoparticles; a potential semiconductor for photoelectric devices. Int. J. Bio-Inorg. Hybr. Nanomater. 5, 115–120.

Erhardt, C.S., Caldeira, L.E., Venturini, J., Bragança, S.R., Bergmann, C.P., 2020. Sucrose as a sol-gel synthesis additive for tuning spinel inversion and improving the magnetic properties of $CoFe_2O_4$ nanoparticles. Ceram. Int. 46, 12759–12766.

Hutchings, G.J., Mirazaei, A.A., Joyner, R.W., Siddiqui, M.R.H., Taylor, S.H., 1996. Ambient temperature CO oxidation using copper manganese oxide catalysts prepared by co-precipitation: effect of ageing on catalyst performance. Catal. Lett. 42, 21–24.

Jeyasubramanian, K., Hikku, G.S., Sharma, R.K., 2015. Photocatalytic degradation of methyl violet dye using zinc oxide nano particles prepared by a novel precipitation method and its antibacterial activities. J. Water Proc. Eng. 8, 35–44.

Khoshkhan, Z., Mirzaei, M., Eshtiagh-Hosseini, H., Izadyar, M., Mague, J.T., Korabik, M., 2021. Two polyoxometalate-based hybrids constructed from trinuclear lanthanoid clusters with single-molecule magnet behavior. Polyhedron 194, 114903.

Larbi, T., Doll, K., Amlouk, M., 2019. Temperature dependence of Raman spectra and first principles study of $NiMn_2O_4$ magnetic spinel oxide thin films. Application in efficient photocatalytic removal of RhB and MB dyes. Spectrochim. Acta A, Mol. Biomol. Spectrosc. 216, 117–124.

Li, L., Jiang, G., Ma, J., 2018. $CuMn_2O_4$/graphene nanosheets as excellent anode for lithium-ion battery. Mater. Res. Bull. 104, 53–59.

Ma, P., Geng, Q., Gao, X., Yang, S., Liu, G., 2016. Solution combustion of spinel CuMn2O4 ceramic pigments for thickness sensitive spectrally selective (TSSS) paint coatings. Ceram. Int. 42, 11966–11973.

Ma, P., Geng, Q., Gao, X., Zhou, T., Yang, S., Liu, G., 2016. Aqueous solution-derived $CuMn_2O_4$ ceramic films for spectrally selective solar absorbers. Ceram. Int. 42, 19047–19057.

Mahdiani, M., Sobhani, A., Salavati-Niasari, M., 2017. Enhancement of magnetic, electrochemical and photocatalytic properties of lead hexaferrites with coating graphene and CNT: Sol-gel auto-combustion synthesis by valine. Sep. Pur. Tech. 185, 140–148.

Mahdiani, M., Sobhani, A., Salavati-Niasari, M., 2019. The first synthesis of $CdFe_{12}O_{19}$ nanostructures and nanocomposites and considering of magnetic, optical, electrochemical and photocatalytic properties. J. Hazard. Mater. 367, 607–619.

Mirzaei, M., Eshtiagh-Hosseini, H., Alipour, M., Frontera, A., 2014a. Recent developments in the crystal engineering of diverse coordination modes (0–12) for Keggin-type polyoxometalates in hybrid inorganic–organic architectures. Coord. Chem. Rev. 275, 1–18.

Mirzaei, M., Eshtiagh-Hosseini, H., Lotfian, N., Salimi, A., Bauzá, A., Deun, R.V., Decadt, R., Barceló-Oliver, M., Frontera, A., 2014b. Syntheses, structures, properties and DFT study of hybrid inorganic–organic architectures constructed from trinuclear lanthanide frameworks and Keggin-type polyoxometalates. Dalton Trans. 43, 1906–1916.

Mohassel, R., Sobhani, A., Salavati-Niasari, M., Goudarzi, M., 2018a. Pechini synthesis and characteristics of Gd_2CoMnO_6 nanostructures and its structural, optical and photocatalytic properties. Spec. Chem. Acta A 204, 232–240.

Mohassel, R., Sobhani, A., Goudarzi, M., Salavati-Niasari, M., 2018b. Amino acid modified combustion synthesis, characterization and investigation of magnetic, optical and photocatalytic properties of Gd_2CoMnO_6 nanostructures. J. Alloy. Compd. 753, 615–621.

Nie, L., Li, S., Chai, S., Han, N., Chen, Y., 2022. Photothermal catalytic oxidation of toluene with enhanced efficiency over constructed $CuMn_2O_4/Mn_2O_3$ heterojunction catalyst. Appl. Sur. Sci. 605, 154567.

Nikhil Chandran, M.K., Suresh Babu, G.N., Sathish, M., 2023. $CuMn_2O_4$ anchored on graphene sheets as a high-performance electrodes for sodium-ion batteries. J. Energy Storage 65, 107346.

Owczarz, P., Orczykowska, M., Rył, A., Ziółkowski, P., 2019. The effects of sucrose on the sol-gel phase transition and viscoelastic properties of potato starch solutions. Food Chem. 271, 94–101.

Pedra, P.P., Silva Filho, J.L., Lima, R.J.S., Sharma, S.K., Moura, K. O., Duque, J.G.S., Meneses, C.T., 2016. The influence of chelating agent on the structural and magnetic properties of $CoFe_2O_4$ nanoparticles. J. Nanosci. Nanotechnol. 16, 4943–4947.

Popescu, I., Boudjemaa, A., Nassima, H., Bessekhouad, Y., Tudorache, M., Bachari, K., Marcu, I.C., 2015. Study of the electrical and catalytic properties of spinels with CuFe2-xMnxO4 composition (x = 0, 0.4, 0.8, 1.6 and 2). Appl. Catal. A: Gen. 504, 29–36.

Ryu, J., Choi, W., 2006. Photocatalytic oxidation of arsenite on TiO_2: understanding the controversial oxidation mechanism involving superoxides and the effect of alternative electron acceptors. Env. Sci. Tech. 40, 7034–7039.

Salunkhe, A.B., Khot, V.M., Phadatare, M.R., Pawar, S.H., 2012. Combustion synthesis of cobalt ferrite nanoparticles-influence of fuel to oxidizer ratio. J. Alloy. Compd. 514, 91–96.

Samadi Kazemi, M., Sobhani, A., 2023. $CuMn_2O_4$/chitosan micro/nanocomposite: Green synthesis, methylene blue removal, and study of kinetic adsorption, adsorption isotherm experiments, mechanism and adsorbent capacity. Arab. J. Chem. 16, 104754.

Samaniyan, M., Mirzaei, M., Gomila, R.M., Eshtiagh-Hosseini, H., Lotfian, N., Mague, J.T., Nakhaei Pour, A., Frontera, A., 2021. Supramolecular network of a framework material supported by the anion–π linkage of Keggin-type heteropolyoxotungstates: experimental and theoretical insights. Dalton Trans. 50, 1895–1900.

Saravanakumar, B., Muthu Lakshmi, S., Ravi, G., Ganesh, V., Sakunthala, A., Yuvakkumar, R., 2017. Electrochemical properties of rice-like copper manganese oxide (CuMn2O4) nanoparticles for pseudocapacitor applications. J. Alloy. Compd. 723, 115–122.

Sobhani, A., 2022. Hydrothermal synthesis of $CuMn_2O_4$/CuO micro composite without capping agent and study its photocatalytic activity for elimination of dye pollution. Int. J. Hydrogen Energy 47, 20138–20152.

Sobhani-Nasab, A., Eghbali-Arani, M., Hosseinpour-Mashkani, S.M., Ahmadi, F., Rahimi-Nasrabadi, M., Ameri, V., 2020. Eco-friendly preparation and characterization of $CuMn_2O_4$ nanoparticles with the green capping agent and their photocatalytic and photovoltaic applications. Iran. J. Catal. 10, 91–99.

Sun, R.I., Zhang, S.R., An, K., Song, P.F., Liu, Y., 2021. $Cu_{1.5}Mn_{1.5}O_4$ spinel type composite oxide modified with CuO for synergistic catalysis of CO oxidation. J. Fuel Chem. Technol. 49, 799–808.

Tang, Z.R., Kondrat, S.A., Dickinson, C., Bartley, J.K., Carley, A.F., Taylor, S.H., Davies, T.E., Allix, M., Rosseinsky, M.J., Claridge, J. B., Xu, Z., Romani, S., Crudace, M.J., Hutchings, G.J., 2011. Synthesis of high surface area $CuMn_2O_4$ by supercritical anti-solvent precipitation for the oxidation of CO at ambient temperature. Catal. Sci. Technol. 1, 740–746.

Verwey, E.J.W., Heilmann, E.L., 1947. Physical properties and cation arrangement of oxides with spinel structures II. electronic conductivity. J. Chem. Phys. 15, 174–180.

Wang, Z., Liu, J., Yang, Y., Yu, Y., Yan, X., Zhang, Z., 2020. AMn2O4 (A = Cu, Ni and Zn) sorbents coupling high adsorption and regeneration performance for elemental mercury removal from syngas. J. Hazard. Mater. 388, 121738–121739.

Wang, L.J., Zhou, Q., Liang, Y., Shi, H., Zhang, G., Wang, B., Zhang, W., Lei, B., Wang, W.Z., 2013. Size effect and enhanced photocatalytic activity of CuO sheet-like nanostructures prepared by a room temperature solution phase chemical method. Appl. Surf. Sci. 271, 136–140.

Wollner, A., Lange, F., Schemelz, H., Knozinger, H., 1993. Characterization of mixed copper-manganese oxides supported on titania catalysts for selective oxidation of ammonia. Appl. Catal. A: Gen. 94, 181–203.

Zhang, W., Au, C., Wan, H., 1998. Active site of praseodymium orthovanadate catalyst in oxidative dehydrogenation of propane. Chin. Sci. Bull. 43, 217–220.